nature portfolio

https://doi.org/10.1038/s41563-021-01166-1

Supplementary information

Competing correlated states around the zero-field Wigner crystallization transition of electrons in two dimensions

In the format provided by the authors and unedited

nature portfolio

https://doi.org/10.1038/s41563-021-01166-1

Supplementary information

Competing correlated states around the zero-field Wigner crystallization transition of electrons in two dimensions

In the format provided by the authors and unedited

Competing correlated states around the zero field Wigner crystallization transition of electrons in two-dimensions

J. Falson,[1,2,3,*] I. Sodemann,[4,5] B. Skinner,[6] D. Tabrea,[1] Y. Kozuka,[7,8] A. Tsukazaki,[9] M. Kawasaki,[10,11] K. von Klitzing,[1] and J. H. Smet[1]

[1]*Max-Planck-Institute for Solid State Research, D-70569 Stuttgart, Germany*
[2]*Department of Applied Physics and Materials Science, California Institute of Technology, Pasadena, California 91125, USA.*
[3]*Institute for Quantum Information and Matter, California Institute of Technology, Pasadena, California 91125, USA*
[4]*Max-Planck-Institute for the Physics of Complex Systems, 01187 Dresden, Germany*
[5]*Institut für Theoretische Physik, Universität Leipzig, D-04103, Leipzig, Germany*
[6]*Department of Physics, Ohio State University, Columbus, Ohio 43210, USA*
[7]*Research Center for Magnetic and Spintronic Materials, National Institute for Materials Science, Tsukuba 305-0047, Japan*
[8]*JST, PRESTO, Kawaguchi, Saitama, 332-0012, Japan*
[9]*Institute for Materials Research, Tohoku University, Sendai 980-8577, Japan*
[10]*Department of Applied Physics and Quantum-Phase Electronics Center (QPEC), University of Tokyo, Tokyo 113-8656, Japan*
[11]*RIKEN Center for Emergent Matter Science (CEMS), Wako 351-0198, Japan*

S1. SAMPLE PARAMETERS

TABLE I: Parameters of the MgZnO/ZnO 2DES when $n = 2.3 \times 10^{10}$ cm^{-2},$m_b = 0.30m_0$ [Ref.1] and $\epsilon = 8.5\epsilon_0$. The electron mobility is assumed to be around $\mu = 600,000$ cm^2/Vs.

Parameter	Magnitude	Units
E_F	1.8×10^{-4}	eV
T_F	2.1	K
τ_{tr}	$\approx 100 \times10^{-12}$	s
τ_q	$\approx 10 \times10^{-12}$	s
L	$\approx 1.7\times10^{-6}$	m
r_s	25	
q_{TF}	1.3×10^{9}	m^{-1}
t_{WF}	$\approx 10 \times10^{-9}$	m
$k_F t_{WF}$	≈ 0.3	

Table I collects relevant parameters of the MgZnO/ZnO 2DES when $n = 2.3 \times10^{10}$ cm^{-2}. Here, E_F the kinetic energy, T_F the Fermi temperature, τ_{tr} the transport scattering time, τ_q the quantum scattering time (estimated from the onset field of quantum oscillations), L the mean free path of carriers, r_s the Wigner-Seitz parameter, q_{TF} the Thomas-Fermi screening wave length, and t_{WF} an estimate of the wavefunction thickness (based on the data presented in Ref.2). Note that the band effective mass is used in these calculations and the value of $m_b = 0.30m_0$ is the mean value of cyclotron resonance measurements in Ref.1. In that work, and uncertainty of $\pm0.01m_0$ was identified, which provides a 3% uncertainty in our calculated value of r_s. The role of renormalized mass values will be discussed in the subsequent sections. The quasi-Hall bar sample is not well suited for accurate calculations of the electron mobility, and hence we work with an assumed peak electron mobility of approximately 600,000 cm^2/Vs. This is calculated based on the measured resistance of the device, which is assumed to be the same order of magnitude as the resistivity. Previous studies[3] reported an electron mobility at $T = 500$ mK of $\mu = 80,000$ cm^2/Vs when $n = 2\times10^{10}$ cm^{-2}. Our results point towards an approximately four times enhancement of the electron mobility when reducing the temperature from 500 mK to approximately 10 mK. The μ =80,000 cm^2/Vs device in Ref.3 would thus translate to a mobility of approximately μ =300,000 cm^2/Vs when n=2 $\times10^{10}$ cm^{-2} at lower temperatures, which is a value comparable to the device studied in this work. Furthermore, as a simple consistency check, the MIT occurs at the $3h/e^2$ in this work, which is comparable to many reports in the literature of a value of h/e^2. Low-field quantum oscillations begin at approximately 0.07 T, yielding a conservative estimate of the quantum lifetime of carriers τ_q >10 ps, using the relationship $\tau_q^{-1} = 2\omega_c$ where ω_c is the cyclotron frequency at the onset of oscillations using the band mass. Furthermore, Ohmic contacts were formed by evaporating Ti (10 nm) followed by Au (50 nm) on the sample surface. Indium was additionally soldered upon these pads to improve the contact quality. Qualitatively similar results were obtained both with and without this additional indium layer.

S2. MEASUREMENT DETAILS

All measurements have taken place in a ^{3}He immersion cell anchored at the base of an annealed silver cold finger attached to the mixing chamber of a 650μW at 120 mK dilution refrigerator (base $T \approx 7$ mK), as shown in Fig.1. The cell design is based on the one utilized at the Na-

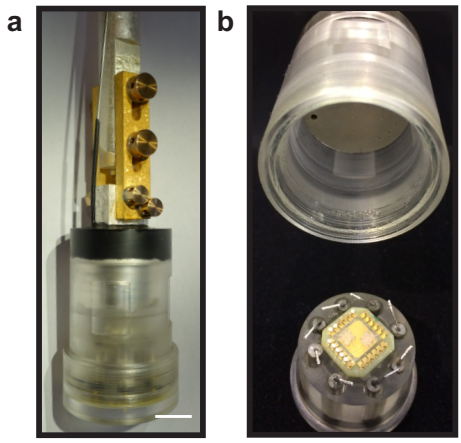

FIG. 1: **The ^{3}He immersion cell. a** Closed cell with sample puck inside (scale bar ≈1 cm) **b** Open cell displaying the main heat exchanger and ^{3}He inlet hole (top) and sample puck (bottom). The sample is glued upon a metalized chip carrier, with each contact being connected to a sintered silver heat exchanger by a gold bonding wire.

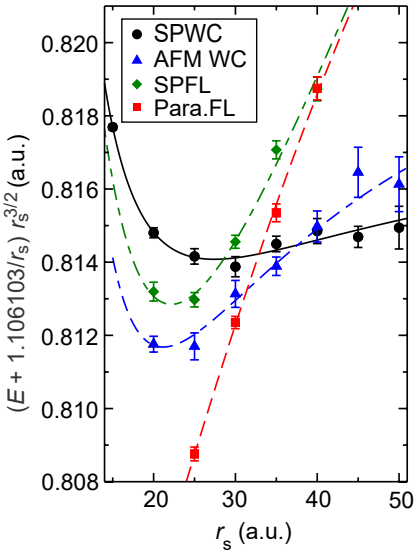

FIG. 2: **Quantum Monte Carlo results adapted from Ref.8.** The energy E per electron of competing unpolarized paramagnetic Fermi liquid (Para. FL), spin polarized Fermi liquid (SPFL), unpolarized AFM Wigner crystal (AFM WC) and polarized Wigner crystal (SPWC) as a function of r_s.

tional High Magnetic Field Laboratory High B/T facility in Gainesville, Florida. This technique has proven powerful in achieving the low electron temperatures required for studies of delicate fractional quantum Hall features,[4,5] and also insulating phases in low density 2DES devices.[6] The mixing chamber temperature is measured using a calibrated cerous magnesium nitrate paramagnetic thermometer for $T \leq 120$ mK, and a ruthenium oxide thermometer for $T \geq 50$ mK. These thermometers have good overlap in the range $50< T <120$ mK. We do not measure the temperature inside the ^{3}He cell. As electrons at low temperature are actively cooled primarily via electrical contacts at ultra-low temperatures, the exact electron temperature is dependent on the contact resistance. The Kapitza phonon interfacial resistance ($\propto 1/(AT^3)$) may be effectively suppressed by immersing the sample in the cryogen and attaching large surface area (A) sintered silver heat exchangers to each measurement wire. Electrical signals are carried from room temperature down to the mixing chamber using individual thermocoax lines, each with a length of approximately 2 m. These lines are thermally anchored at the 1 K, still, 50 mK and mixing chamber plates. These cables act as distributed R-C filters and are effective in attenuating stray radiation in cryogenics applications.[7] They consist of a resistive stainless steel inner conductor ($R_{\rm cable} \approx 150\,\Omega$) isolated from the outer conductor by a MgO nanoparticle dielectric. The skin effect of the nanoparticles strongly attenuates high frequency signals (> 1 MHz). An additional R-C filter is employed at the mixing chamber. Superconducting Nb-Ti loom is used between the mixing chamber and the measurement puck.

Magnetic flux is generated by a 3-axis (9-3-1 T) superconducting vector magnet. The cryostat is suspended above a pit carved into a 35 ton concrete block that is subsequently isolated from the main building structure by vibration dampening pads. Circulation pumps are anchored to the outer wall of the superstructure to reduce vibrations. The measurement room is electrically isolated from the outside environment by a Faraday cage delivering -60 dBm attenuation. Measurement electronics are powered by a dedicated phase of a three-phase power supply, operate on individual isolating transformers, and are isolated from the data gathering measurement computer by an optical isolator. Significant efforts, such as electrically isolating the cryostat from pumps and diagnostics electronics, have been taken to minimize ground-loops within the measurement circuitry. We strive to utilize low-noise electronics for measurements, such as all analogue lock-in amplifiers (PAR 124A) (only used for the data presented in Fig.11), Yokogawa 7651 DC voltage sources and DL Instruments voltage (1201) and current (1211) preamplifiers.

DC measurement techniques often incorporate offsets in both the current and voltage signal. These offsets can also fluctuate in time. We have tried to reduce this uncertainty by ensuring excellent temperature stability of the laboratory, while maintaining electrical power to the electronics at all times. The current offset is addressed by adjusting the zero offset of the current preamplifier at zero applied electric field. The voltage offsets are more challenging to eliminate with features order of nano- to microvolts between individual IV sweeps being observed. The only point where we have adjusted the data in this manuscript is in Fig.4**a-c** and 15, where we take the measured voltage at zero current at a set temperature and charge density and subtract it as an offset for each trace.

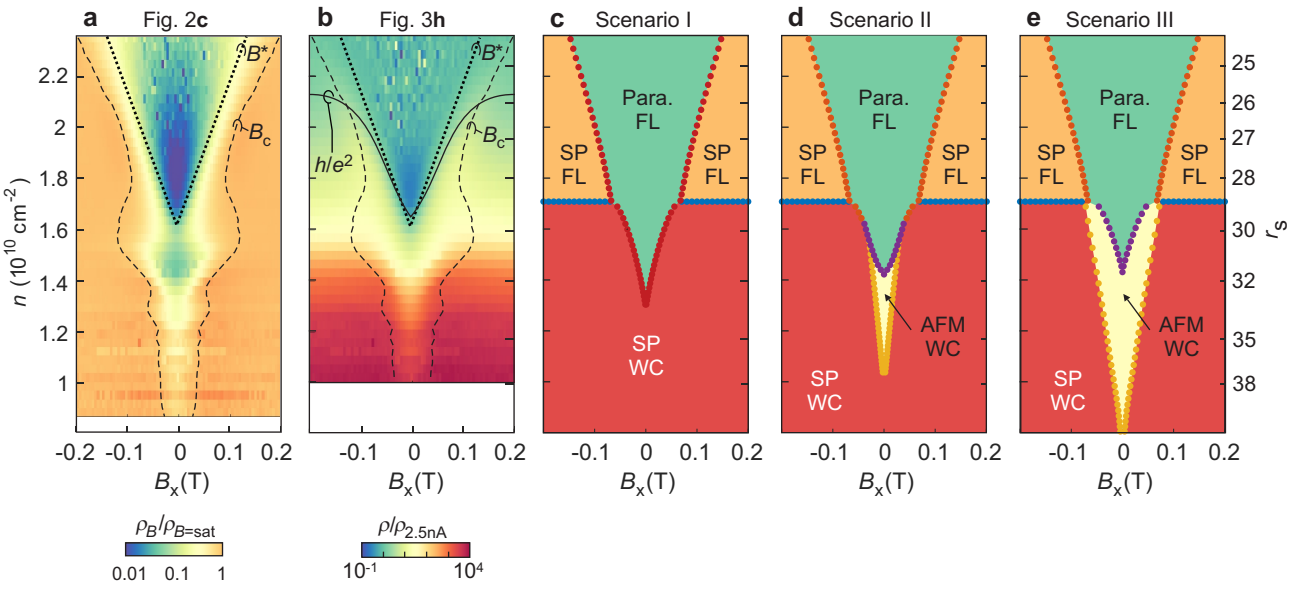

FIG. 3: **Comparison of experimental data with QMC ground states.**[8] **a** $\rho_{\rm B}/\rho_{\rm B=sat}$ in the (B_x,n)-plane. **b** Nonlinearity in IV, defined as $\rho/\rho_{2.5\rm nA}$ in the (B_x,n)-plane. Phases associated with **c** scenario I, **d** scenario II and **e** scenario III, as discussed in Sec. S3 A.

The process of differentiating data eliminates this offset as it is only sensitive to the slope of the data.

S3. MONTE-CARLO PHASE DIAGRAMS OF 2D JELLIUM

The analysis we present here relies on the variational Monte-Carlo study of Ref.8. This study compared energies of four states: a spin unpolarized paramagnetic Fermi liquid (Para. FL), spin polarized Fermi liquid (SP FL), spin unpolarized Wigner crystal (AFM WC) with a stripe-like spin antiferromagnetic order and a triangular lattice and a spin polarized Wigner crystal (SP WC) with triangular lattice. The main results of Ref.8 are adapted in Fig. 2, and imply that as r_s increases, the ground state progresses from Para. FL, to AFM WC, to SP WC, in the vicinity of $r_{\rm s}=30$. Importantly, Ref.8 ruled out the possibility of the traditional Stoner transition from Para. FL to a SP FL.

We use this study to estimate the phase diagram as a function $B_{\|}$ and r_s. Because electrons in ZnO have weak spin-orbit coupling, the total spin S_z of the system is a good quantum number. This allows us to know the exact energy of each of the four states previously described, which are all either fully spin polarized or fully spin unpolarized. However, to have a complete phase diagram we need to estimate the energy of potential states with different partial polarization. To do this, it is unavoidable to make certain assumptions about the dependence of the energy on spin polarization. We therefore analyze the competition of these phases within three distinct scenarios. As we will see the main conclusions are relatively robust to the assumptions within different scenarios.

A. Scenario I: phase diagrams without a partially polarized crystal

The appearance of a possible competing intermediate crystal is a relatively new development within the series of Monte-Carlo studies of the ideal Jellium model,[8] although indications of such an intermediate state appeared in a previous study,[9] and also in self-consistent Hartree-Fock calculations.[10,11] Since most previous studies did not find or ignored the possibility of these partially polarized crystalline states, it is natural to try to determine what would be the phase diagram if such states are not considered as part of the competing states. To do so we begin by approximating the ground state energy per electron of the Fermi liquids as a function of their spin polarization polarization p, given by

$$p \equiv \frac{n_\uparrow - n_\downarrow}{n_\uparrow + n_\downarrow},\ p \in [-1,1], \tag{S1}$$

with a simple parabolic dependence, as follows:

$$\epsilon_{FL} \approx \epsilon_{Para.FL}(r_s) + p^2(\epsilon_{SPFL}(r_s) - \epsilon_{Para.FL}(r_s)) - \frac{g\mu_B B_x}{2}p. \tag{S2}$$

Here $\epsilon_{Para.FL}$ and ϵ_{SPFL} are the energies of the unpolarized FL and spin polarized FL phases from Ref.8 and the g-factor is $g \approx 2$.[12] Notice from Fig. 2 that since $\epsilon_{Para.FL}(r_s) < \epsilon_{SPFL}(r_s)$ for our range of interest $r_{\rm s} \lesssim 40$, there is always an energy penalty for polarizing the Fermi liquid, and no Stoner transition. In this first scenario, these states compete only with a PWC, whose

energy is

$$\epsilon_{WC} \approx \epsilon_{SPWC}(r_s) - \frac{g\mu_B|B_x|}{2}, \tag{S3}$$

where ϵ_{SPWC} is the energy of spin polarized WC from Ref.8. For each r_s we find the FL state with the optimal polarization and determine its energy competition with the WC. The resulting phase diagram is shown in Fig. 3**c**.

B. Scenario II: phase diagrams with a partially polarized crystal with a first order transition

We now include the possibility of a partially polarized (AFM) WC and model its energy using the same parabolic dependence we used for the FL, as follows:

$$\epsilon_{WC} \approx \epsilon_{AFMWC}(r_s) + p^2(\epsilon_{SPWC}(r_s) - \epsilon_{AFMWC}(r_s)) - \frac{g\mu_B B_x}{2}p \tag{S4}$$

The phase diagrams obtained by comparing these energies from those of the FL states from Eq. (S2) is shown in Fig. 3**d**. Notice that since there is a crossing of the energies of SPWC and AFM WC around $r_s \approx 38$ (see Fig. 2), the above form predicts a first-order spin-flop-type transition of the spin polarization among the WC states at $r_s \approx 38$. There is *a priori* no reason favoring this transition to be first order rather than continuous, which leads us to consider this scenario separately.

C. Scenario III: phase diagrams with a partially polarized crystal with a continuous transition

In order to account for a possible continuous transition of the spin polarization of the partially polarized Wigner crystal into the fully polarized crystal, we parameterize their energy dependence on spin polarization with a simple quartic Ginzburg-Landau (GL) form:

$$\epsilon_{WC} \approx \epsilon_{AFMWC}(r_s) + p^2 b(r_s) + p^4 c(r_s) - \frac{g\mu_B B_x}{2}p \tag{S5}$$

As customary for GL quartic functionals, we take the coefficient $c(r_s)$ to be positive for all r_s. The crystal starts developing a non-zero spontaneous spin-polarization at a certain density r_{s1}, for which the coefficient $b(r_s)$ changes from positive to negative. For $r_s > r_{s1}$ the GL functional predicts a monotonically increasing spontaneous polarization, until the system saturates at $p = 1$ at some second density r_{s2}. With these inputs the coefficients of the GL functional can be fixed to be:

$$b(r_s) = 2(\epsilon_{AFMWC}(r_s) - \epsilon_{AFMWC}(r_{s1})) \times \frac{\epsilon_{AFMWC}(r_{s2}) - \epsilon_{SPWC}(r_{s2})}{\epsilon_{AFMWC}(r_{s2}) - \epsilon_{SPWC}(r_{s1})}, \tag{S6}$$

$$c(r_s) = \epsilon_{SPWC}(r_s) - \epsilon_{AFMWC}(r_s) - b(r_s). \tag{S7}$$

Since the Monte Carlo study[8] did not explore partially polarized states, the precise values of r_{s1} and r_{s2} are unknown, although they should satisfy $r_{s1} < 38 < r_{s2}$. The phase diagram shown in Fig. 3**e** has been made by choosing $r_{s1} = 27$ and $r_{s2} = 45$. The precise of form of the phase diagram does not have strong sensitivity on the precise values of r_{s1} and r_{s2}, provided they are chosen in the vicinity of $r_s \sim 38$ up to some distance of about $\Delta r_s \sim 10$. In fact, in the limiting case in which the polarization changes rapidly from unpolarized to polarized, r_{s1} approaches r_{s2} and one recovers the Scenario II of a first order transition. The main difference is a reduction in size of the region where the partially polarized crystal is energetically favored, but the overall shape of the two phase diagrams still looks reasonably similar in both scenarios II and III, shown in Fig. 3**d** and **e**.

S4. LANDAU FERMI LIQUID PARAMETERS

The energy density of the metallic system at fixed density in the presence of an in-plane Zeeman field, B_x, is given by

$$E \approx E_0 + \frac{s_z^2}{2\chi} - g_0\frac{\mu_B}{\hbar}s_z B_x + \mathcal{O}(s_z^4), \tag{S8}$$

where $s_z = (\hbar/2)(n_\uparrow - n_\downarrow)$ is the spin density, $\chi = m^*/4\pi$ the spin susceptibility, g_0 is the g-factor, and μ_B is the Bohr magneton. Therefore, the critical field, B_c, at which the system fully spin polarizes at a given total density, $s_z^{\rm pol} = (\hbar/2)n$, provides an approximate measure of the spin susceptibility of the system:

$$B_c \approx \frac{\hbar^2 n}{2\mu_B}\frac{1}{g_0\chi}. \tag{S9}$$

Notice that because the dependence of energy of the electron system on spin polarization is not strictly a parabola, the measured χ inferred from the above formula is not strictly speaking the differential susceptibility at B=0, but rather a finite difference susceptibility characterizing the energy cost to fully spin polarize the paramagnetic electron fluid. However, these two susceptibilities can be shown to be identical in the case of the free electron gas, and are expected to be close to each other in general whenever the electron system has energy density that is a smooth function of the spin polarization. In Landau Fermi liquid theory, this susceptibility is expressed in terms of the quasiparticle mass (m^*), the bare band mass (m_b), the bare spin susceptibility (χ_0) and the $F_s(0)$ Landau parameter as follows[13]:

$$\chi = \chi_0\frac{1}{1+F_s(0)}\frac{m^*}{m_b}. \tag{S10}$$

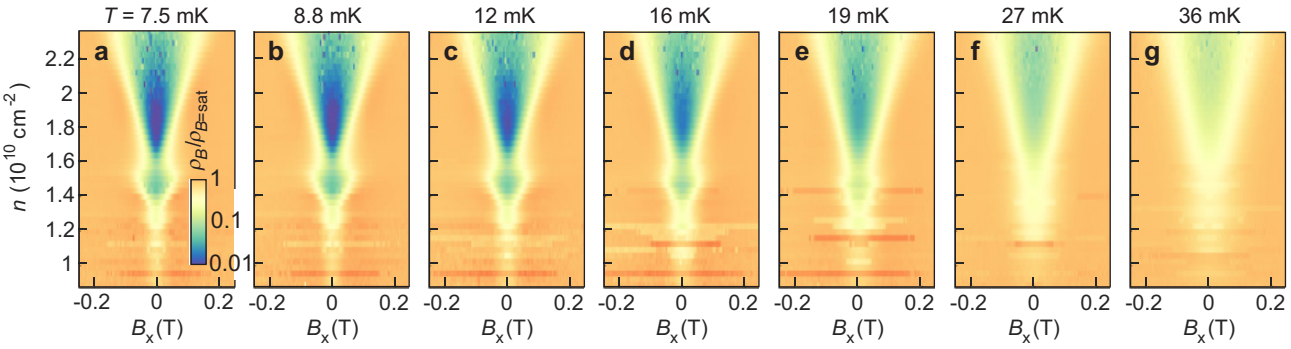

FIG. 4: **Temperature dependence of in-plane magnetic field mapping. a-g** Mapping of the normalized differential resistance $\rho/\rho_{\mathrm{B=sat}}$ as a function of B_{x} and n at different temperatures.

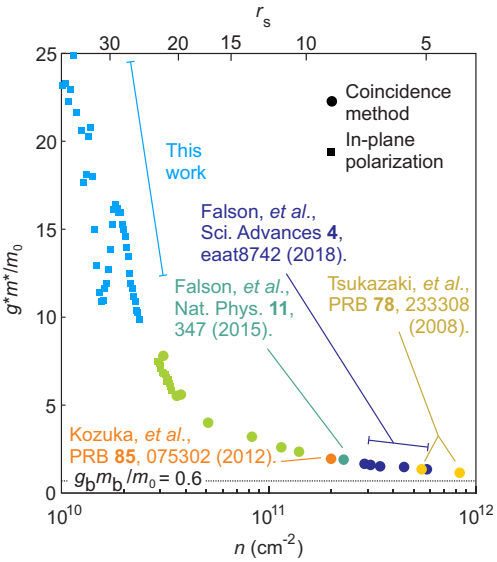

FIG. 5: **Summary of renormalization effects in ZnO devices.** g^*m^*/m_0 as a function of n. The band value $g_{\mathrm{b}}m_{\mathrm{b}}/m_0$=0.6 is displayed as a horizontal dashed line. Data have been gathered from devices analyzed in this text, previous publications,[14–17] and other unpublished measurements.

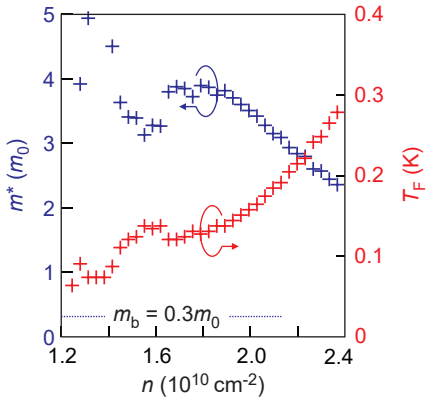

FIG. 6: Estimated renormalized effective mass and Fermi temperature as a function of n. See text and also Ref.18 for an extended discussion.

The spin susceptibility of carriers can be evaluated by various means. A strategy we have employed in previous studies is the coincidence method which relies on rotating the sample within a magnetic field to study transport features associated with the crossing of opposing spin Landau levels.[14,16,17] In addition to the coincidence method, it is possible to polarize carriers into a single spin band by applying an in-plane magnetic field. According to Eq.S9, identification of a critical field B_{c} leads to the quantification of g^*m^*/m_0. This measurement is discussed in the main text in the context of Fig. 3 with saturation of the magnetoresistance at a critical field B_{c} being taken as evidence for full spin polarization.

For the sake of completeness, here we present the full raw data set used to produce the analysis presented in Fig. 3 of the main text. This data set comprises multiple maps of the differential resistance in the (n,B_{x})-parameter space at a number of set temperatures. These are all presented in Fig. 4. As in Fig. 3**b**, we plot the ratio $\rho/\rho_{\mathrm{B=sat}}$, where $\rho_{\mathrm{B=sat}}$ is the saturated differential resistance at a set charge density at high magnetic field (corresponding to full spin polarization). The characteristic positive magnetoresistance is evident for all T at high n, but is difficult to discern in the higher $T > 20$ mK data upon depletion of the 2DES.

The renormalization of band parameters in the ZnO-based 2DES as a function of charge density is summarized in Fig. 5. This figure is compiled from values reported in previous publications,[15–17] the devices presented in this manuscript, along with other unpublished results gathered on samples characterized in the course of this project. Values obtained through the coincidence method are displayed as circles, with squares representing those gained through analyzing the positive magnetoresistance of a polarizing in-plane magnetic field. The error associated with each point is no larger than the symbol size. A good agreement between these two methods is obtained for the range of densities shown. We additionally display the corresponding r_{s} value at each n on the top axis. Previous studies on Si-based devices identified that the enhancement of the spin susceptibility as the critical density is approached is associated with an enhancement of

the effective mass.[19] The matter of parameter enhancement is a widely studied property and discussed in more detail in Refs.20,21.

Utilizing the experimentally obtained g^*m^*/m_0 we can estimate the renormalized Fermi temperature (T_F^*) as a function of n. This is plotted in Fig. 6. We stress that we have not directly measured m^* in this study, for example through temperature dependent measurements of Shubnikov-de Haas oscillations. Rather, this is a value calculated working under the assumption that the density dependent enhancement of g^*m^*/m_0 is primarily due to the renormalization of the effective mass, with an assumed constant value of g^* that was found to be enhanced by a factor of 2, as was discussed in Ref.18 We also refer the reader to Ref.1 for a comparison between approaches to measuring the renormalized and non-renormalized effective mass in ZnO. A local "peak" in $\partial\rho/\partial T|_n$ of dilute 2DES emerges[22–24] as T becomes comparable but smaller than T_F given $T < T_{BG}$, where $T_{BG}=2k_F\hbar v_s/k_b \approx 2.4$ K is the Bloch-Grüneissen temperature calculated using $v_s = 4400$ m/s as the average between transverse and longitudinal sound velocities in ZnO and $n = 2\times10^{10}$ cm^{-2}. Being deep in the Bloch-Grüneissen regime, phonon scattering contributes little to the resistivity. A local peak in $\partial\rho/\partial T|_n$ is an experimental feature is observed in our data for $n > 1.6\times10^{10}$ cm^{-2}. The calculated T_F^* values are those presented in Fig.9**a**. The local maximum in $\rho(T)$ when $n > n_c$ occurs just below the calculated T_F^*. We note that the corresponding calculated Fermi temperature is in the range $T_F = 1.5 \sim 1.7$ K utilizing the band mass.

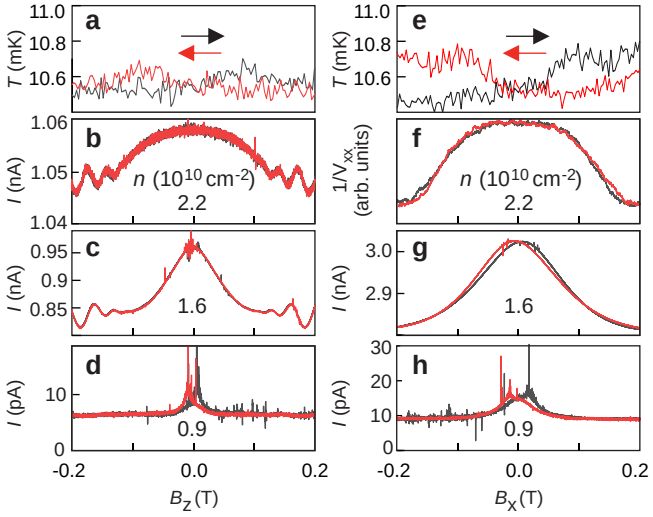

FIG. 7: **Sweep direction dependent magnetotransport in the vector magnet equipped cryostat. a** Temperature read at the mixing chamber plate as a function of sweep dependence for an out-of-plane magnetic field (B_z). **b-d** Measured electrical characteristics for three different charge densities. Panels **e-h** plot analogous data with the magnetic field projected in the in-plane direction (B_x).

S5. ABSENCE OF MAGNETOSTATICALLY INDUCED HYSTERESIS AND DOMAINS IN FERROMAGNETIC PHASES

Here we estimate the typical value of the coercive fields associated with magnetic hysteresis arising from magneto-static fields. Our goal is to argue that these fields are too small to be responsible for any observed behavior in our samples. We clarify that our argument does not imply that the system cannot, in principle, display hysteresis via other mechanisms, such as metastability associated with pinning of the Wigner crystal. But we are able to argue that the non-trivial in-plane field dependence of the resistivity of the insulating state, seen in Fig.3**b** of main text, cannot be a result of magnetic-field-induced ferromagnetic domain alignment of the putative ferromagnetic Wigner crystal.

Since ZnO has negligible spin-orbit coupling, the formation of magnetic domains and hysteresis is dictated by magneto-statics. Assuming that each electron contributes one Bohr magneton, μ_B, to the magnetization in the spin polarized state, the coercive field scale (the magnetic field width of hysteresis loop) can be estimated to be:

$$B_c = \mu_0\mu_B\frac{1}{V_{elec}} = \mu_0\mu_B\frac{n}{d}, \tag{S11}$$

where μ_0 is the vacuum magnetic permeability constant, $V_{elec} = d/n$ is the average volume per electron, and $d \approx 5$ nm is the effective well width of the 2DES in ZnO. For $n \sim 10^{10}cm^{-2}$ we have:

$$B_c \sim 2.4\times10^{-7}\text{T}. \tag{S12}$$

The smallness of this scale is ultimately a consequence of the tremendous diluteness of our systems. Each electron occupies a 3D volume of about $V_{elec} \sim 5\times10^7$ Å^3, which is about 5×10^6 larger than in ordinary 3D metals such as copper. The above strongly indicates that magnetostatic domain formation is completely negligible.

We now present our experimental data close to zero field for the sake of completeness. After much effort to properly understand these effects, we emphasize that it is extremely difficult to eliminate all parasitic effects when collecting the data. There are a number of experimental unknowns that are difficult to avoid. Firstly we mention temperature fluctuations when sweeping the magnetic field due to the presence of nuclear and electron spin magnetization processes. These may occur in the sample, electrical contacts, experimental wiring, and materials used to construct the helium immersion cell. Furthermore, it is very difficult to exclude the influence of remnant magnetic flux in the superconducting magnet system used.

Figure 7 presents sweep-direction-dependent electrical characteristics of the device measured. The sample is biased with a DC voltage that produces approximately

1 nA when charge is accumulated and the sample is metallic. Panels **a-d** present data when the field is projected in the z direction, with **e-g** presenting data in the x direction. We measure the thermometer reading at the mixing chamber through these sweeps, which are performed at a very low rate of 1 mT/min, as shown in panels **a** and **e**. Sweeping B_z conveniently reveals quantum oscillations, whose period are known to be determined by the magnetic flux penetrating the sample, and therefore may be used to reduce the uncertainty of remnant flux in the coil at low field by forcing the oscillation minima in up-sweep and down-sweep data to overlap. Panels **b-d** and **f-h** present sweeps at three distinct charge densities, corresponding to the metallic, critical and insulating portions of the parameter space. Within our detection limit, the up- and down-sweep data overlap closely, as shown in panel **b**. Operating under the assumption that hysteresis is weak or absent at this charge density, we enforce up- and down-sweep data to overlap measured in the $B_{\rm x}$ direction, as shown in panel **f**. This process establishes a remnant flux of approximately 5 mT in the $B_{\rm z}$ and 15 mT in the $B_{\rm x}$ coils. This value is used to manually offset subsequent field sweeps performed in a repetitive cycle in an attempt to reduce the impact of this parasitic effect. Next, we can vary the charge density of the device, as plotted in panels **c** and **g** when n is close to $n_{\rm c}$. While higher field quantum oscillations overlap nicely in the B_z data set, additional delicate features close to $B = 0$ in the form of sharp spikes in the data are resolved in both projections of the magnetic field. These become even more evident upon reducing n below $n_{\rm c}$. While these features occur at fields where the temperature read during up and down sweeps coincides, it is not possible for us to know what is occurring locally at the sample. These features do not follow a Curie-Weiss-like temperature dependence and are robust only when the $|d\rho/dT|$ of the device is high. Hence, in the absence of direct spin-sensitive probes and an estimate of the coercive field, we associate the hysteresis with an uncontrollable experimental aspect of the measurement.

S6. EXCHANGE SCALE ESTIMATE AND IMPACT OF TEMPERATURE FLUCTUATIONS ON SPIN ORDER

To estimate the typical scale of the spin exchange energy of the Wigner crystal, J, we will compare the energy difference per electron of the AFM WC and the FM WC obtained from QMC in Ref.8. In Fig. 8 we plot this energy difference in units of mK, by using parameters relevant for ZnO, given by $m_{\rm b} \approx 0.30 m_0$, $\epsilon \approx 8.5$, as a function of r_s. We also display horizontal dashed lines corresponding to a temperature scale $T = 10$mK. We see that the energy difference never exceeds this temperature scale over the entire range of $r_s \in [30, 45]$, and in particular, it is clearly smaller than this scale in the Ferromagnetic side. This suggests that our experimental

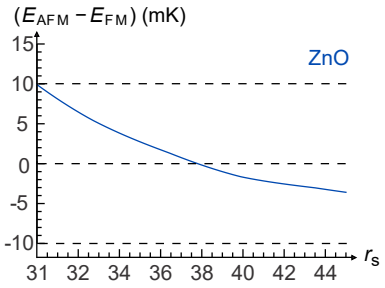

FIG. 8: Energy difference per electron of the AFM WC and FM WC from QMC,[8] with parameters adjusted for ZnO in units of mK.

temperatures are at best only comparable with the scale needed to destroy the spin ordering of the WC at $B_x = 0$ and therefore temperature fluctuations are presumably playing an important role in disordering the spins even at the lowest temperatures we reach experimentally. This qualitative conclusion is not affected even after accounting for the error bars in Fig.3, that amount to an uncertainty on the energy difference of about 4 mK at $r_s \approx 45$, where the error bars are larger.

If one would plot the same energy difference as that in Fig.8 but for the microscopic parameters of AlAs two-dimensional electron systems studied in Ref.,[25] by taking $m_{\rm b} \approx 0.4 m_0$, and $\epsilon \approx 10$, one would obtain essentially the same absolute energy scales and the same figure. This is because the effective Hartree energy scale $\hbar^2/ma^2$ is nearly identical in both systems and approximately about $1260K$ (here a denotes the effective Bohr radius). However, since the lowest temperature reached in Ref.25 was $T \approx 300$mK, it is unlikely that their system reaches the regime of ferromagnetic ordering. We note that AlAs and ZnO have very important differences in their microscopic Hamiltonians, most notably AlAs has a band mass anisotropy of about $m_x/m_y \approx 5$. It is also important to bear in mind that the energy differences between the several competing states in the in the vicinity of $r_s \approx 30$ is very small (on the order of $10^{-5}\hbar^2/(m_{\rm b}a^2)$), and therefore such important differences could quite naturally lead to a different phase diagram in comparison to ZnO. Bearing this in mind, we would like, however, to offer another potential explanation for their observations at the lowest densities of in-plane field. It is possible that the apparent absence of notable magnetoresistance as a function of $B_{\rm x}$ might no longer be a reliable criterion for establishing spin polarization deep in the insulating regime at such elevated temperatures. As we see in our case, even a relatively modest increase of the temperature to about $T = 40$ mK, is enough to flatten out the magnetoresistance as a function of Bx at the lowest densities (see e.g. Fig.3**c** of main text and Fig.4). It is therefore possible that their magnetoresistance traces that were taken at at $T \approx 300$ mK will display some dependence on $B_{\rm x}$ at lower temperatures in the low density insulating regime.

S7. TEMPERATURE DEPENDENCE OF THE RESISTANCE

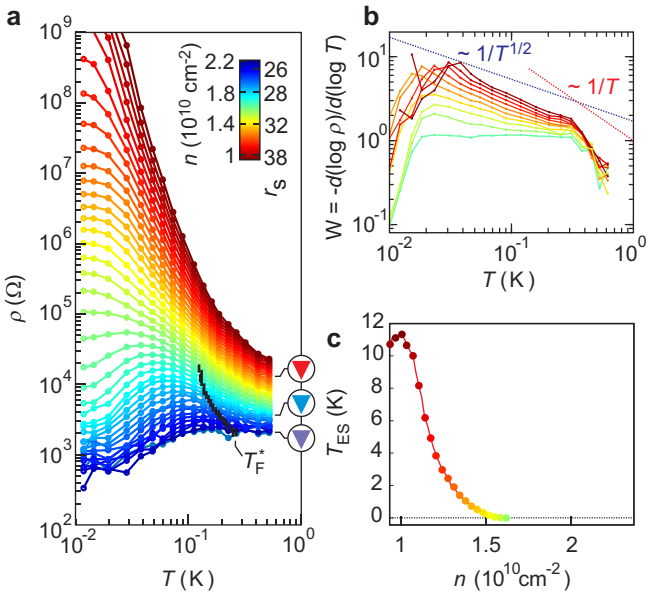

FIG. 9: **Temperature dependent transfer characteristics. a** MIT in the temperature dependence of the resistance as n is tuned. **b** $T_{\rm ES}$ as a function of n. **c** Estimated activation energy ΔE as a function of electron density n, obtained by fitting the temperature range 300 mK $< T <$ 700 mK.

We divide the data presented in Fig. 9**a** into separate regimes of temperature in order to perform an analysis of the temperature dependence of the resistance. In this section we first discuss the behavior at zero magnetic field before turning to the behavior at $B_x > B_c$.

A. Zero magnetic field

In electronic insulating phases, the temperature-dependent resistivity is generically described by

$$\rho(T) \propto \frac{1}{T^{\alpha}} \exp\left[\left(\frac{T_0}{T}\right)^{\beta}\right]. \qquad \text{(S13)}$$

At low temperatures the exponent β dominates the behavior of the resistance, and it can take a range of values depending on the mechanism for transport. These include $\beta = 1$ for Arrhenius-type activated transport, $\beta = 1/2$ for Coulomb-gap mediated variable range hopping, and $\beta = 1/3$ for Mott-like variable range hopping.[26] A common method for estimating the exponent β is to perform a Zabrodskii-Zinov'eva analysis,[27] in which one defines the (dimensionless) reduced activation energy

$$W(T) = -\frac{d\ln\rho}{d\ln T} = \beta\left(\frac{T_0}{T}\right)^{\beta} + \alpha. \qquad \text{(S14)}$$

The analysis in Fig. 9**b** suggests that at $n < n_c$ there exists a regime of $\beta = 1/2$ at low temperature that crosses over to a regime of $\beta = 1$ at higher temperature, as in conventional semiconductors on the insulating side of the doping-induced metal-insulator transition.[26] (It is particularly difficult to extract reliable estimates of $W(T)$ at $T \lesssim 20$ mK due to possible decoupling of the electron temperature from that of the cryogen.) Within the regime of $\beta = 1/2$, the value of the temperature T_0 (which can be called the "Efros-Shklovskii temperature" $T_{\rm ES}$) depends on the localization length ξ as $T_{\rm ES} = 6.2e^2/(4\pi\epsilon k_B\xi)$.[26] We observe that $T_{\rm ES}$ vanishes as the electron density approaches $n = n_c$ from below (Fig. 9**c**), which is consistent with a divergence of the localization length at the metal-insulator transition.

An alternative and more direct analysis for assessing the temperature dependence of potentially insulating states is to perform a fit to the form of Eq. S13 over all regimes of temperature and density for which $d\rho/dT < 0$ (the usual definition of "insulating-like" temperature dependence). Upon close inspection, such a regime appears for all n; it is weak but notable even at our maximum value of n under the condition $T > T_{\rm F}^*$. Figure 10**a** plots $\ln\rho$ as a function of $1/T$ at a number of n at zero magnetic field. The solid lines represent individual fits at discrete n. For this process, we avoid using the lowest temperature data points in the strongly insulating regime owing to our inability to exactly determine the electron temperature as the base temperature T is approached, and also due to experimental difficulties associated with determining $dV_{\rm xx}/dI$ at very low currents in strongly non-linear $I-V$ traces. Figure 10**c** plots β as a function of n. The exponent β is small (insulating-like behavior is weak) at $n > n_{\rm c}$, but rises rapidly as $n_{\rm c}$ is reduced below $n_{\rm c}$. The value of β ultimately appears to saturate at a value of approximately $\beta \approx 0.65$ at the lowest n.

We separately examine the metallic regime $n < n_{\rm c}$, for which we fit the data according to a power law,

$$\rho(T) \propto T^{\gamma}. \qquad \text{(S15)}$$

For this analysis, we restrict the range of temperatures to approximately 16 mk $< T < 0.8T_{\rm F}|_n$. This is the temperature scaling of the degenerate liquid when $T < T_{\rm F}^*$. We exclude the lowest temperature data points as we are unable to verify that the electron temperature of the sample is accurately reflected by the thermometer based at the mixing chamber at very low temperatures. Figure 10**b** presents a log-log plot of the data illustrating a gradually changing slope (*i.e.* γ) as n is tuned. The value obtained is plotted as red in Fig. 10**c**. It can be gauged that $\rho(T)$ is approximately linear in T (γ=1) when $n \approx 2\times10^{10}$ cm^{-2}, with γ trending towards a value of 1.6 with decreasing n immediately before the onset of the MIT. At lower n metallicity is rapidly suppressed, and the insulating behavior becomes prominent for all T.

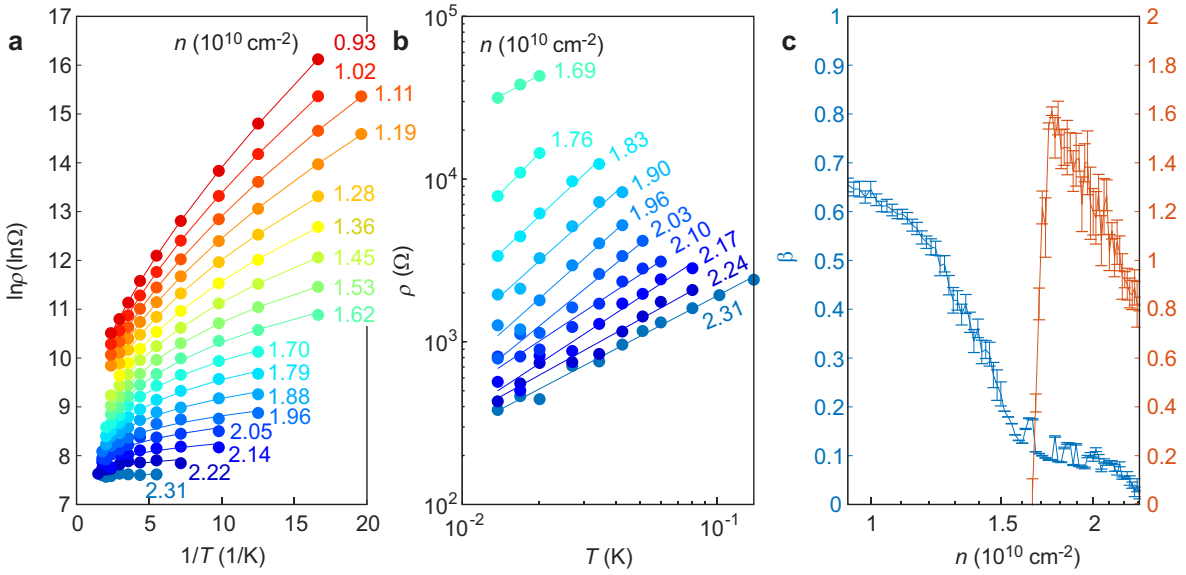

FIG. 10: Temperature scaling analysis in **a** the insulating and **b** the metallic regime. **c** Summary of temperature scaling exponents.

B. Evolution with in-plane field

As discussed above, applying an in-plane magnetic field acts to polarize the 2DES into a single spin band. Previous measurements in silicon-based devices have suggested that in-plane field also produces an apparent field-induced MIT at an intermediate partial spin polarization.[28] We examine this effect in Fig. 11 by plotting the longitudinal resistance as a function of B_x at various T. Here, we present AC measurements recorded at a current of 2 nA. Panels **a-c** present the raw magnetotransport data at three distinct n. It is possible to identify a change in the sign of $d\rho/dT$ at a finite field B^*, at which all the temperature curves coincide. The value of B^* is identified as an open circle in Fig. 11 at both polarities of the field. Tracking the value of B^* as a function of n gives the results plotted in panel **d**. Extrapolating this value to $B^* = 0$ gives a density 1.6×10^{10} cm^{-2} at zero field, which coincides with the value of n_c obtained by DC measurements and discussed in the main text.

In the regime of larger-than-critical density, $n > n_c$, and large in-plane field, $B > B_c$, the 2DES exhibits insulating-like temperature dependence $d\rho/dT$. However, the form of the temperature dependence in this regime is somewhat weaker than in the regime of $n < n_c$ discussed above. This weak dependence can be seen in Fig. 11**e**, which shows that the conductivity σ increases roughly linearly with temperature (rather than exponentially). Such a linear dependence is qualitatively consistent with a perturbative calculation by Zala et. al.,[29,30] who found that the conductivity of a spin-polarized FL has a positive, linear-in-T correction due to electron-electron interactions. The reduced activation energy $W(T)$ in this regime (and at $T \gtrsim 20$ mK) is also consistent with $W(T) = \text{const.}$ (Fig. 11**f**).

S8. DISORDER-INDUCED DENSITY MODULATION

The phases of the 2DES are generally discussed in terms of a spatially uniform electron density n. But when the 2DES is subjected to disorder in the form of stray electric charges, these charges create a random electric potential that modulates the density of the 2DEG spatially. As mentioned in the main text, this modulation allows for the possibility of multiple phases coexisting in different regions of the sample. In reality, both interaction effects and disorder are important factors determining the ground state of the system, and the nonlinear transport features of the insulating phase are likely emerging from a pinned WC with short range order.

A typical source of disorder for a 2DES is a finite concentration of uncontrolled impurity charges embedded three-dimensionally in the substrate. Due to the long-ranged nature of the Coulomb interaction, such impurity charges produce an arbitrarily large variation in the electrostatic potential over sufficiently long length scales, even when their bulk concentration $N_{\rm imp}$ is very small, unless they are screened by the 2DES itself. So long as $N_{\rm imp}$ is sufficiently small (discussed below), this screening can be described using the Thomas-Fermi approximation.[31] The corresponding root-mean-square variation $(\delta n)^2$ in electron concentration is given by[32]

$$\delta n = \sqrt{\frac{e^4 N_{\rm imp}}{4\pi\epsilon}\left|\frac{dn}{d\mu}\right|}. \qquad \text{(S16)}$$

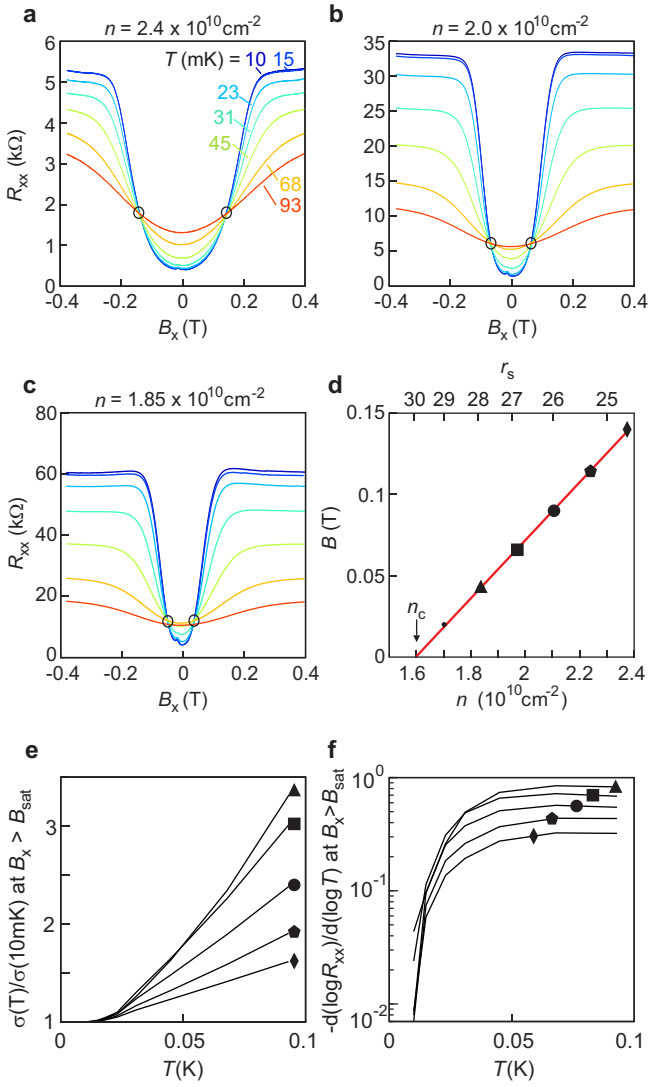

FIG. 11: **Estimate of the critical carrier density n_c through temperature dependent in-plane magnetic field sweeps.** Panels **a-c** AC magnetotransport sweeps (I_{AC} = 2 nA) recorded from positive to negative polarity field. The colors correspond to temperatures noted in panel **a**. Open circles correspond to the field-induced change in temperature dependence. **d** The identified magnetic field for the change in temperature dependence as a function of n. A linear regression through the experimental points (black dots) results in an estimation of the critical carrier density for the zero field MIT occurring at $n_c = 1.6\times10^{10}$ cm^{-2}. **e** Temperature dependence of the normalized conductivity for charge densities studied in panel **d**. **f** Zabrodskii-Zinov'eva analysis.[27]

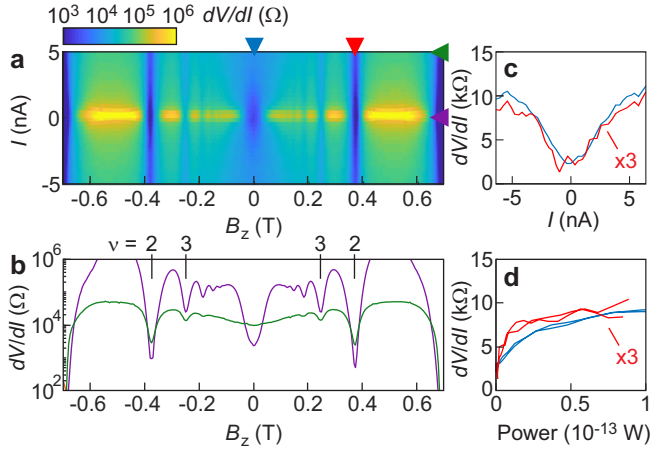

FIG. 12: **Examination of the role of current heating recorded at base temperature of the cryostat. Here, n=1.8×10^{10} cm^{-2}.** **a** Mapping of magnetotransport in the (B_z,I)-plane. **b** Line cut of the transport taken at I=0 nA (purple) and 5 nA (green). **c** dV/dI as a function of I at B_z=0 T (blue) and 0.375 T (red, corresponding to ν=2). **d** dV/dI as a function of dissipated power ($P = IV$), also recorded at B_z=0 T (blue) and 0.375 T (red).

The quantity $dn/d\mu$ represents the thermodynamic density of states (μ denotes the chemical potential), and can be either positive or negative, depending on the strength of electron correlations.[33–36]

For the strongly-interacting states that we are considering, $dn/d\mu$ is of order $4\pi\epsilon n^{1/2}/e^2$ in magnitude, and consequently

$$\delta n \sim (N_{\rm imp}^2 n)^{1/4}. \tag{S17}$$

For our MgZnO/ZnO heterostructures, the bulk impurity concentration is estimated to be below 10^{14} cm^{-3},[37] so that the corresponding density modulation satisfies

$$\delta n \lesssim 0.3\times10^{10}\ {\rm cm}^{-2}. \tag{S18}$$

The Thomas-Fermi approximation that we have employed in this section is valid so long as the typical distance between impurity charges, $N_{\rm imp}^{-1/3}$, is much longer than the Thomas-Fermi screening radius $(2\epsilon/e^2)(d\mu/dn)$, which in our case amounts to $N_{\rm imp} \ll n^{3/2}$. This inequality is easily satisfied in our devices.

S9. HEATING

It is difficult to quantify the extent to which heating influences electrical transport characteristics at very low temperatures. Heating can appear through both current-induced Joule heating (proportional to I^2R in an Ohmic system), as well as magnetic processes as the polarity of the applied magnetic field is changed. From our experiences in higher charge density devices ($n = 2 \sim 5\times10^{11}$ cm^{-2}) with similar geometries, such as those studied in Refs. [16,17,38], Joule heating is negligible in the analysis of fractional quantum Hall energy gaps for currents below approximately 10 nA. However, the charge density, resistivity, and proximity to the MIT of the device under study here puts it in a different parameter space, necessitating a reevaluation of the role of current-induced heating.

Figure 12 examines the role of current-induced Joule heating by examining transport in the (B_z,I)-plane. Panel **a** renders the differential resistance as a function of perpendicular field and current, with two line cuts being presented in panel **b**. Integer quantum Hall features are visible as vertical deep blue lines in panel **a**, and deep minima in panel **b**. The U-shaped magnetoresistance is evident in the purple trace ($I \to 0$ nA), but less so in the finite current trace (green, $I \approx 5$ nA). Conventionally, quantum Hall features exhibit an activated temperature dependence ($\rho \propto \exp(\Delta_\mu/T)$), where Δ_μ is the activation gap of the state. The depth of the minimum is strongly dependent on temperature, becoming deeper as T is reduced. We leverage this character to evaluate the role of current-induced heating. Two traces of ρ as a function of I are presented in panel **c**. The blue trace corresponds to $B_z = 0$ T, with the red trace taken at the $\nu = 2$ minimum $B_z = 0.375$ T). n is chosen in a way that the $\nu = 2$ minimum is finite and should be sensitive to any increase in temperature. The data in panel **c** shows ρ increases by a factor of approximately three when increasing the current to 5 nA. The data taken at zero field (blue) reveal a notably similar character.

At this charge density ($n = 1.8\times10^{10}$ cm^{-2}), ρ reaches 10 kΩ when we heat the mixing chamber to be $T_{\rm MC} \approx$ 80 mK. A heating power approaching 300 μW applied to the mixing chamber plate is required in order to achieve that temperature at the thermometer. Panel **d** takes ρ and plots it as a function of dissipated power across voltage probes ($P = IV$). It is difficult to predict the exact relationship between ρ and power owing to the complicated temperature dependence of the 2DES and thermal coupling of the device to cryogenics surfaces. We remark that the power dissipated inside the samples is 10 orders of magnitude smaller than the equivalent power required at the mixing chamber plate. While our transport measurements preclude detailed conclusions about the texture of carriers inside the device, we speculate that conventional Joule heating of a homogeneous liquid could not be responsible for this increase in ρ.

Finally, we note that the non-linear $I - V$ characteristics, along with a dramatic decrease in ρ at low T saturating to a non-zero value is reminiscent of recently reported experimental features obtained in van der Waals-based two-dimensional systems in close proximity to an insulating phase.[39,40]

S10. METHODS FOR DETERMINING B_c

The uncertainty involved in the quantification of B_c at very low field values results in deviations in the calculated value of χ. This uncertainty has quantitative impacts on the results discussed in Fig. 3, but does not change the overall physical picture discussed in this manuscript. For the sake of completeness, here we discuss identification of B_c using three different methods. The second derivative of ρ with respect to B exhibits a local minimum in the vicinity of B_c, which can be used to identify its value. This approach may be systematically applied to analyze the data and obtain $B_c(n)$. An example of the raw data and second derivative is presented in Fig. 13**a**. It is visually apparent that the local minimum in $d^2\rho/dB^2$ occurs at a value of B_x that is close to where the positive magnetoresistance saturates. A second method for estimating B_c is based on fitting a linear slope to log $\rho(B)$ in the positive magnetoresistance regime. B_c is defined as the point at which the extrapolated value of this slope is equal to the saturated resistance at high B ($\rho_{\rm B=sat}$). An example is displayed in Fig. 13**b** as the blue trace. Finally, the framework in Ref. [41] provides a third method for extracting B_c using the magnetoconductivity data. In this method, B_c is identified with the crossover between a linear fit of $\sigma(B)$ and the value σ_∞ at $B_x \to \infty$. This third method is demonstrated in Fig. 13**b** via the red trace.

The results of these three quantification approaches are displayed in Fig. 13**c** and **d**. While some systematic discrepancy is evident between the three methods, they each produce the same qualitative features, including: 1) a steady decrease (increase) of B_c (g^*m^*/m_0) as n is reduced from above n_c, 2) an alteration of this trend at approximately $n = n_c$, and 3) an apparent saturation of B_c/n as when $n \ll n_c$.

S11. TEMPERATURE AND FIELD DEPENDENCE OF EXCESS CONDUCTANCE

The excess conductance identified in Fig. 2 bears some resemblance to other anomalous metal phases discussed in the literature.[42] In such systems, the longitudinal resistivity falls at low temperature as if approaching a superconducting ground state, only to saturate at a finite value. This saturation is accompanied by strong positive magnetoresistance. Our results, along with others present in other studies,[43,44] identify this excess conductance occurring immediately prior to the MIT at zero field. Figure 14 presents an extended data set taken at $n = 1.82\times10^{10}$ cm^{-2} in the device reported in this work. Panels **a** and **b** present dV/dI at various temperatures as a function of I at $B = 0.25$ and 0 T, respectively. A transition from a zero-electric-field insulating state to the excess conductance phase is evident between these two conditions. The former occurs when the 2DES is fully spin polarized, as discussed above. This is clear based on an examination of panel **c**, where ρ is plotted as a function of B_x, and is seen to saturate above $|B_x| \approx 0.07$ T. Panels **d-f** map dV/dI in the (B_x,I)–plane at three distinct temperatures. The excess conductance phase is observed at low $|B|$ and $|I|$ as a blue region at low temperature. The insulating phase emerges above B_c and is restricted to low $|I|$. By $T = 36$ mK both of these features are largely washed out.

S12. TWO-POINT CURRENT-VOLTAGE CHARACTERISTICS

Data presented throughout the main text and previous supplementary information sections have all been gathered in a four-point measurement geometry, as shown in Fig.1**a**. Figure 15 presents data from the same experimental procedure performed to gather the data of Fig. 2, only taken in a two-point configuration. Here, current is supplied to the device through the sample contacts used to measure the voltage drop, as shown in the upper schematic of Fig. 15. The voltage preamplifier is connected after the load resistor ($R = 10$ MΩ) at the break-out box. The signal therefore contains a contribution from the measurement wires (approximately 150Ω each direction) and contact resistance of the device. The data in Fig. 15 qualitatively reproduce the result presented in Fig.4 of the main text. The data confirms that the contacts are ohmic for all n when $T > 100$ mK.

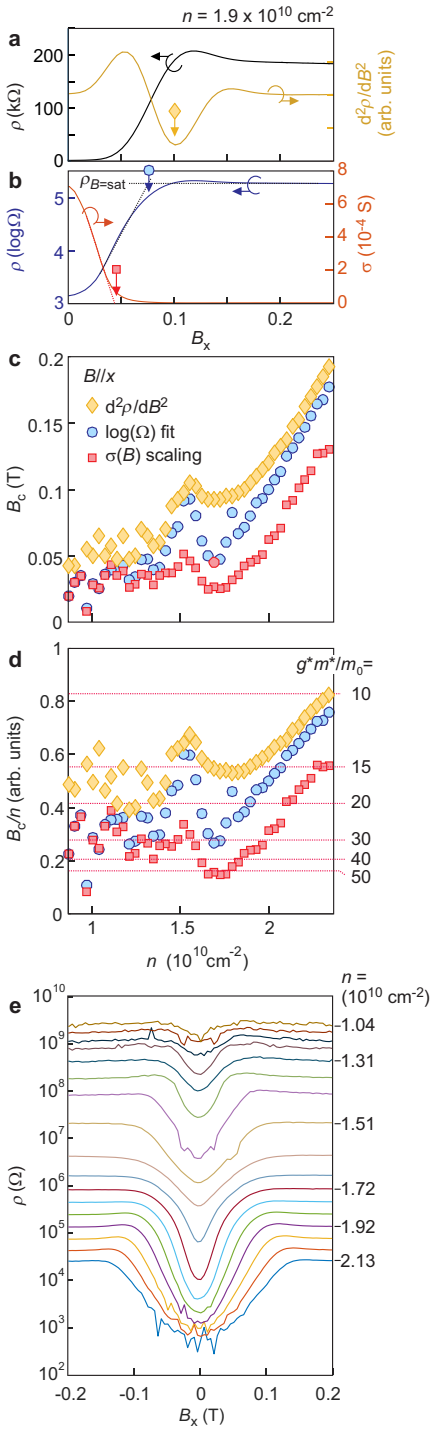

FIG. 13: **Comparison of B_c from multiple approaches.** Here, $n = 1.9{\times}10^{10}$ cm^{-2}. **a** ρ and $d^2\rho/dB^2$ as a function of B_x. The orange diamond highlights the minimum in the second derivative used to quantify B_c. **b** ρ plotted on a log scale and $\sigma(B)$ as a function of B_x. The blue circle and red square highlight B_c for these respective traces. **c** B_c and **d** ratio of B_c/n as a function of n for these three approaches. The corresponding g^*m^*/m_0 is indicated to the right hand side of panel **d**. **e** Raw data traces at set charge densities. $T \approx 10$ mK for all data.

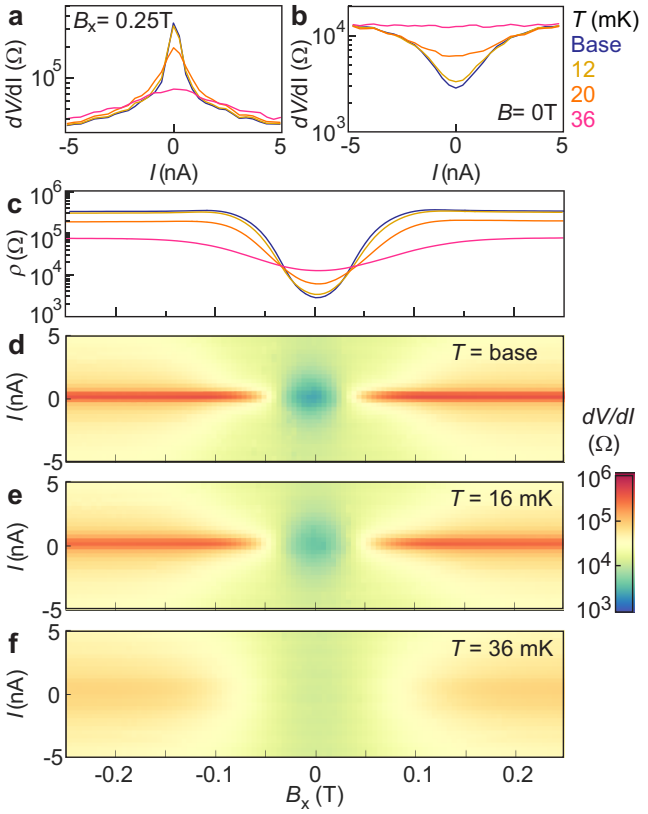

FIG. 14: **Examination of excess conductivity.** Here, n=1.82×10^{10} cm^{-2}. Temperature dependence of dV/dI as a function of I at **a** B_x=0.25 T and **b** B_x=0 T. **c** ρ as a function of B_x. The measurement temperature is indicated outside the right hand side of panel **b**. Panels **d-f** map dV/dI in the (B_x,I)-plane at three distinct temperatures.

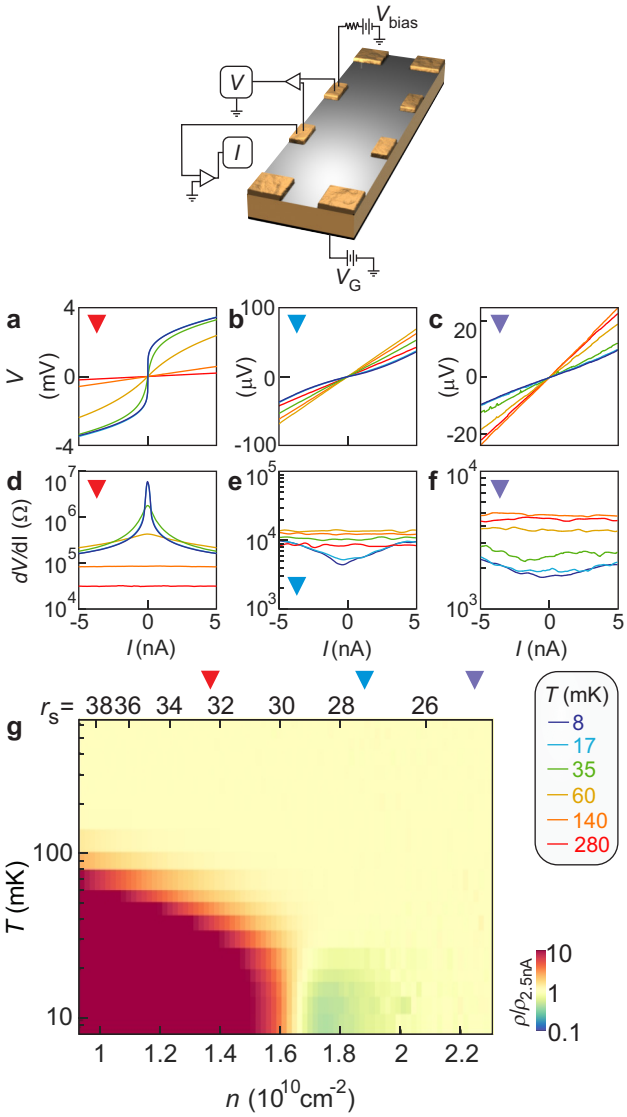

FIG. 15: **Charge transport characteristics in a two-point measurement geometry. a-c** I-V sweeps at various T when n=1.38, 1.91, and 2.26×10^{10} cm^{-2}. **d-f** First differential (dV/dI) of the I-V characteristics for the same set of temperatures. **g** Non-linearity, defined as $\rho/\rho_{2.5\mathrm{nA}}$ in the current-voltage characteristics of the device as a function of n and T. Colored triangles highlight the three regimes discussed in the text and their location on panel **g**.

* Electronic address: falson@caltech.edu

[1] D. Tabrea, I. A. Dmitriev, S. I. Dorozhkin, B. P. Gorshunov, A. V. Boris, Y. Kozuka, A. Tsukazaki, M. Kawasaki, K. von Klitzing, and J. Falson, Phys. Rev. B **102**, 115432 (2020), URL https://link.aps.org/doi/10.1103/PhysRevB.102.115432.

[2] V. V. Solovyev, A. B. Van'kov, I. V. Kukushkin, J. Falson, D. Zhang, D. Maryenko, Y. Kozuka, A. Tsukazaki, J. H. Smet, and M. Kawasaki, Applied Physics Letters **106**, 082102 (2015), https://doi.org/10.1063/1.4913313, URL https://doi.org/10.1063/1.4913313.

[3] J. Falson and Y. Kozuka and M. Uchida and J. H Smet and T. Arima and A. Tsukazaki and M. Kawasaki, Scientific reports **6**, 26598 (2016).

[4] W. Pan, J.-S. Xia, V. Shvarts, D. E. Adams, H. L. Stormer, D. C. Tsui, L. N. Pfeiffer, K. W. Baldwin, and K. W. West, Phys. Rev. Lett. **83**, 3530 (1999), URL https://link.aps.org/doi/10.1103/PhysRevLett.83.3530.

[5] N. Samkharadze, A. Kumar, M. J. Manfra, L. N. Pfeiffer, K. W. West, and G. A. Csáthy, Review of Scientific Instruments **82**, 053902 (2011), https://aip.scitation.org/doi/pdf/10.1063/1.3586766, URL https://aip.scitation.org/doi/abs/10.1063/1.3586766.

[6] T. Knighton, Z. Wu, J. Huang, A. Serafin, J. S. Xia, L. N. Pfeiffer, and K. W. West, Phys. Rev. B **97**, 085135 (2018), URL https://link.aps.org/doi/10.1103/PhysRevB.97.085135.

[7] A. B. Zorin, Review of Scientific Instruments **66**, 4296 (1995), https://doi.org/10.1063/1.1145385, URL https://doi.org/10.1063/1.1145385.

[8] N. D. Drummond and R. J. Needs, Phys. Rev. Lett. **102**, 126402 (2009), URL https://link.aps.org/doi/10.1103/PhysRevLett.102.126402.

[9] B. Bernu, L. Cândido, and D. M. Ceperley, Phys. Rev. Lett. **86**, 870 (2001), URL https://link.aps.org/doi/10.1103/PhysRevLett.86.870.

[10] B. Bernu, F. Delyon, M. Holzmann, and L. Baguet, Phys. Rev. B **84**, 115115 (2011), URL https://link.aps.org/doi/10.1103/PhysRevB.84.115115.

[11] B. Bernu, F. Delyon, L. Baguet, and M. Holzmann, Contributions to Plasma Physics **57**, 524 (2017), https://onlinelibrary.wiley.com/doi/pdf/10.1002/ctpp.201700139, URL https://onlinelibrary.wiley.com/doi/abs/10.1002/ctpp.201700139.

[12] Y. Kozuka, S. Teraoka, J. Falson, A. Oiwa, A. Tsukazaki, S. Tarucha, and M. Kawasaki, Phys. Rev. B **87**, 205411 (2013), URL https://link.aps.org/doi/10.1103/PhysRevB.87.205411.

[13] D. Pines, *Theory of Quantum Liquids: Normal Fermi Liquids* (CRC Press, 2018).

[14] A. Tsukazaki, A. Ohtomo, M. Kawasaki, S. Akasaka, H. Yuji, K. Tamura, K. Nakahara, T. Tanabe, A. Kamisawa, T. Gokmen, et al., Phys. Rev. B **78**, 233308 (2008), URL https://link.aps.org/doi/10.1103/PhysRevB.78.233308.

[15] Y. Kozuka, A. Tsukazaki, D. Maryenko, J. Falson, C. Bell, M. Kim, Y. Hikita, H. Y. Hwang, and M. Kawasaki, Phys. Rev. B **85**, 075302 (2012), URL https://link.aps.org/doi/10.1103/PhysRevB.85.075302.

[16] J. Falson, D. Maryenko, B. Friess, D. Zhang, Y. Kozuka, A. Tsukazaki, J. H. Smet, and M. Kawasaki, Nature Physics **11**, 347 (2015).

[17] J. Falson, D. Tabrea, D. Zhang, I. Sodemann, Y. Kozuka, A. Tsukazaki, M. Kawasaki, K. von Klitzing, and J. H. Smet, Science Advances **4**, eaat8742 (2018).

[18] J. Falson and M. Kawasaki, Reports on Progress in Physics **81**, 056501 (2018).

[19] A. A. Shashkin, S. V. Kravchenko, V. T. Dolgopolov, and T. M. Klapwijk, Phys. Rev. B **66**, 073303 (2002), URL https://link.aps.org/doi/10.1103/PhysRevB.66.073303.

[20] S. V. Kravchenko and M. P. Sarachik, Reports on Progress in Physics **67**, 1 (2003), URL https://doi.org/10.1088/0034-4885/67/1/r01.

[21] V. T. Dolgopolov, Physics-Uspekhi **62**, 633 (2019), URL https://doi.org/10.3367/ufne.2018.10.038449.

[22] M. P. Lilly, J. L. Reno, J. A. Simmons, I. B. Spielman, J. P. Eisenstein, L. N. Pfeiffer, K. W. West, E. H. Hwang, and S. Das Sarma, Phys. Rev. Lett. **90**, 056806 (2003), URL https://link.aps.org/doi/10.1103/PhysRevLett.90.056806.

[23] S. Das Sarma and E. H. Hwang, Phys. Rev. B **68**, 195315 (2003), URL https://link.aps.org/doi/10.1103/PhysRevB.68.195315.

[24] S. D. Sarma and E. Hwang, Scientific reports **5**, 1 (2015).

[25] M. S. Hossain, M. K. Ma, K. A. V. Rosales, Y. J. Chung, L. N. Pfeiffer, K. W. West, K. W. Baldwin, and M. Shayegan, Proceedings of the National Academy of Sciences **117**, 32244 (2020), ISSN 0027-8424, https://www.pnas.org/content/117/51/32244.full.pdf, URL https://www.pnas.org/content/117/51/32244.

[26] B. I. Shklovskii and A. L. Efros, *Electronic Properties of Doped Semiconductors* (Springer-Verlag, New York, 1984).

[27] A. Zabrodskii and K. Zinov'eva, JETP **59**, 425 (1984), URL http://www.jetp.ac.ru/cgi-bin/e/index/e/59/2/p425?a=list.

[28] A. A. Shashkin, S. V. Kravchenko, and T. M. Klapwijk, Phys. Rev. Lett. **87**, 266402 (2001), URL https://link.aps.org/doi/10.1103/PhysRevLett.87.266402.

[29] G. Zala, B. N. Narozhny, and I. L. Aleiner, Phys. Rev. B **65**, 020201 (2001), URL https://link.aps.org/doi/10.1103/PhysRevB.65.020201.

[30] G. Zala, B. N. Narozhny, and I. L. Aleiner, Phys. Rev. B **64**, 214204 (2001), URL https://link.aps.org/doi/10.1103/PhysRevB.64.214204.

[31] T. Ando, A. B. Fowler, and F. Stern, Reviews of Modern Physics **54**, 437 (1982), publisher: American Physical Society, URL https://link.aps.org/doi/10.1103/RevModPhys.54.437.

[32] B. Skinner and B. I. Shklovskii, Physical Review B **87**, 075454 (2013), publisher: American Physical Society, URL https://link.aps.org/doi/10.1103/PhysRevB.87.075454.

[33] M. S. Bello, E. I. Levin, B. I. Shklovskii, and A. L. Efros, Sov. Phys. JETP **53**, 822 (1981).
[34] J. P. Eisenstein, G. S. Boebinger, L. N. Pfeiffer, K. W. West, and S. He, Phys. Rev. Lett. **68**, 1383 (1992), URL https://link.aps.org/doi/10.1103/PhysRevLett.68.1383.
[35] J. P. Eisenstein, L. N. Pfeiffer, and K. W. West, Phys. Rev. B **50**, 1760 (1994), URL https://link.aps.org/doi/10.1103/PhysRevB.50.1760.
[36] B. Skinner and B. I. Shklovskii, Phys. Rev. B **82**, 155111 (2010), URL https://link.aps.org/doi/10.1103/PhysRevB.82.155111.
[37] Q. Li, J. Zhang, J. Chong, and X. Hou, Applied Physics Express **6**, 121102 (2013), URL https://doi.org/10.7567/apex.6.121102.
[38] D. Maryenko, A. McCollam, J. Falson, Y. Kozuka, J. Bruin, U. Zeitler, and M. Kawasaki, Nature communications **9**, 4356 (2018).
[39] G. Chen, A. L. Sharpe, P. Gallagher, I. T. Rosen, E. J. Fox, L. Jiang, B. Lyu, H. Li, K. Watanabe, T. Taniguchi, et al., Nature **572**, 215 (2019).
[40] M. He, Y. Li, J. Cai, Y. Liu, K. Watanabe, T. Taniguchi, X. Xu, and M. Yankowitz, Nature Physics (2020).
[41] S. A. Vitkalov, H. Zheng, K. M. Mertes, M. P. Sarachik, and T. M. Klapwijk, Phys. Rev. Lett. **87**, 086401 (2001), URL https://link.aps.org/doi/10.1103/PhysRevLett.87.086401.
[42] A. Kapitulnik, S. A. Kivelson, and B. Spivak, Rev. Mod. Phys. **91**, 011002 (2019), URL https://link.aps.org/doi/10.1103/RevModPhys.91.011002.
[43] S. V. Kravchenko, D. Simonian, M. P. Sarachik, W. Mason, and J. E. Furneaux, Phys. Rev. Lett. **77**, 4938 (1996), URL https://link.aps.org/doi/10.1103/PhysRevLett.77.4938.
[44] J. Yoon, C. C. Li, D. Shahar, D. C. Tsui, and M. Shayegan, Phys. Rev. Lett. **82**, 1744 (1999), URL https://link.aps.org/doi/10.1103/PhysRevLett.82.1744.